

## Electromagnetic wave imaging of three-dimensional targets using a hybrid iterative inversion method

This article has been downloaded from IOPscience. Please scroll down to see the full text article.

2012 Inverse Problems 28 065007

(<http://iopscience.iop.org/0266-5611/28/6/065007>)

View [the table of contents for this issue](#), or go to the [journal homepage](#) for more

Download details:

IP Address: 194.167.230.229

The article was downloaded on 01/05/2012 at 07:41

Please note that [terms and conditions apply](#).

# Electromagnetic wave imaging of three-dimensional targets using a hybrid iterative inversion method

Emeric Mudry, Patrick C Chaumet<sup>1</sup>, Kamal Belkebir and Anne Sentenac

Institut Fresnel (UMR 6133), Aix-Marseille Université, Av Escadrille Normandie-Niemen,  
F-13397 Marseille Cedex 20, France

E-mail: [patrick.chaumet@fresnel.fr](mailto:patrick.chaumet@fresnel.fr)

Received 24 November 2011

Published 27 April 2012

Online at [stacks.iop.org/IP/28/065007](http://stacks.iop.org/IP/28/065007)

## Abstract

In microwave or optical wave imaging set-ups, the measured scattered field is usually not linearly linked to the target parameter of interest. To reconstruct the latter, nonlinearized or linearized iterative inversion techniques, such as the contrast source inversion method (CSI) or the conjugate gradient method (CGM) have been proposed (Litman and Crocco 2009 *Inverse Problems* **25** 020201–5). In this paper, we adapt to the three-dimensional vectorial case, a hybrid method (HM) that combines the advantages of the CSI and CGM, and compare the performances of the different approaches using microwave experimental data. The HM appears to be the best compromise in terms of reconstruction accuracy, computation time and robustness to noise.

(Some figures may appear in colour only in the online journal)

## 1. Introduction

During the past two decades, intense research activity has allowed the emergence of many methods for solving inverse scattering problems in different areas of physics. The aim of inverse scattering problems is to determine properties (location, shape and constitutive material) of unknown targets from the knowledge of their response (scattered field) to a known excitation. Generally, these problems are ill-posed and nonlinear. There exist several ways to solve inverse scattering problems. Most popular strategies that address these problems are iterative, e.g., starting from an initial guess, the parameter of interest is adjusted gradually by minimizing a cost functional involving the measured scattered field data. We distinguish two main approaches, linearized and nonlinearized techniques, depending on whether the field in the scattering domain is considered as fixed (solution of the direct problem for the best available estimation of the parameter) at each iteration step [2–5] or as an unknown that is obtained

<sup>1</sup> Author to whom correspondence should be addressed.

together with the parameter by the minimization procedure [6, 3, 7]. We present herein a hybrid method (HM) that combines advantages of the two approaches and we investigate its performances in the three-dimensional vectorial electromagnetic imaging framework. More precisely, in our imaging configuration, the target is illuminated by an electromagnetic wave and its scattered field is measured along many observation directions. The inverse problem amounts to reconstructing the target three-dimensional permittivity from the set of diffracted field maps obtained under various illuminations.

## 2. Formulation of the forward scattering problem

Let  $\mathbf{E}^0$  be the electric field associated with an electromagnetic wave impinging on an arbitrary object. The incident field induces a polarization inside the object. The macroscopic electric field inside the object satisfies the self-consistent equation [8]

$$\mathbf{E}(\mathbf{r}) = \mathbf{E}^0(\mathbf{r}) + \int_V \mathbf{G}(\mathbf{r}, \mathbf{r}') \chi(\mathbf{r}') \mathbf{E}(\mathbf{r}') d\mathbf{r}', \quad (1)$$

where the integration is performed over the volume of the object.  $\mathbf{E}(\mathbf{r}')$  is the macroscopic field inside the object,  $\chi(\mathbf{r}')$  is the linear susceptibility of the object:

$$\chi(\mathbf{r}') = \varepsilon(\mathbf{r}') - \varepsilon_b, \quad (2)$$

with  $\varepsilon(\mathbf{r}')$  the relative permittivity of the object,  $\varepsilon_b$  the relative permittivity of the vacuum, and  $\mathbf{G}(\mathbf{r}, \mathbf{r}')$  the free-space electric field susceptibility tensor. To solve numerically equation (1) we discretize the object into a set of  $N$  subunits arranged on a cubic lattice, and we assume that the electromagnetic field and the field susceptibility tensor is uniform over one subunit. This approximation is accurate enough to model the scattering of the electromagnetic wave by an object as long as the subunit is smaller than the wavelength within the object and the radiative reaction term is not needed. This latter condition is mandatory for instance when one deals with optical forces [9, 10]. The macroscopic field at each subunit position may be rewritten as

$$\mathbf{E}(\mathbf{r}_i) = \mathbf{E}^0(\mathbf{r}_i) + \sum_{j=1}^N \mathbf{G}(\mathbf{r}_i, \mathbf{r}_j) \chi(\mathbf{r}_j) d^3 \mathbf{E}(\mathbf{r}_j), \quad (3)$$

where the free-space electric field susceptibility tensor is of the form [11]

$$\mathbf{G}(\mathbf{r}_i, \mathbf{r}_j) = e^{ik_0 R} \left[ \left( 3 \frac{\mathbf{R} \otimes \mathbf{R}}{R^2} - \mathbf{I} \right) \left( \frac{1}{R^3} - \frac{ik_0}{R^2} \right) + \left( \mathbf{I} - \frac{\mathbf{R} \otimes \mathbf{R}}{R^2} \right) \frac{k_0^2}{R} \right] - \frac{\mathbf{I}}{3} \delta(\mathbf{R}), \quad (4)$$

where  $\mathbf{R} = \mathbf{r}_i - \mathbf{r}_j$ ,  $k_0$  is the wavenumber of the vacuum,  $d$  is the edge length of the lattice,  $\otimes$  is the tensorial product and  $\mathbf{I}$  is the unit tensor. The linear system represented by equation (3) is solved numerically thanks to a bi-conjugate-type method [12, 13], and the scattered field at any position  $\mathbf{r}$  outside the object is computed using

$$\mathbf{E}^d(\mathbf{r}) = \sum_{j=1}^N \mathbf{G}(\mathbf{r}, \mathbf{r}_j) \chi(\mathbf{r}_j) d^3 \mathbf{E}(\mathbf{r}_j). \quad (5)$$

## 3. Formulation of the inverse scattering problem

The geometry of the problem investigated in this paper is illustrated in figure 1(a). Assume that an unknown three-dimensional object is entirely confined in a bounded box  $\Omega \subset \mathbb{R}^3$  (test domain or an investigating domain) and illuminated successively by  $l = 1, \dots, L$

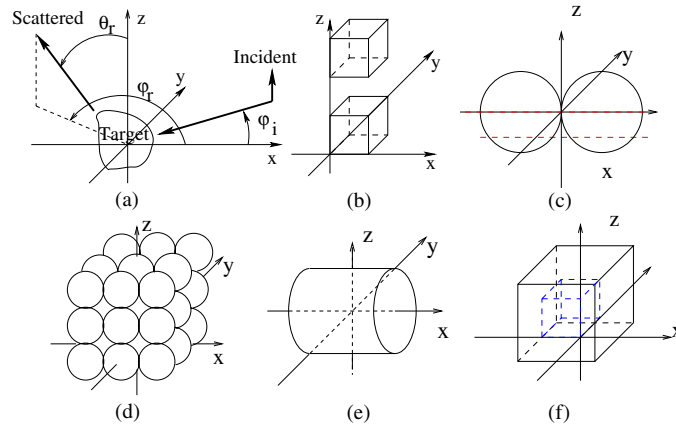


**Figure 1.** (a) Sketch of the experimental set-up. The illumination is done on the  $(x, y)$  plane with  $\varphi_i$  from  $0^\circ$  to  $350^\circ$  step  $10^\circ$ . The polarization of the incident field is along the  $z$ -direction. The receiver position  $\varphi_r$  from  $20^\circ$  to  $340^\circ$  step  $40^\circ$  and  $\theta_r$  from  $-60^\circ$  to  $60^\circ$  step  $15^\circ$ . (b)–(f) are the five different targets under study. (b) Two dielectric cubes of relative permittivity  $\varepsilon = 2.4$  and side  $a = 2.5$  cm located at  $(a/2, a/2, a/2)$  and  $(a/2, a/2, 5a/2)$ . (c) Two spheres in contact with relative permittivity  $\varepsilon = 2.6$  and radius  $r = 2.5$  cm. The centers of the spheres are located at  $(-r, 0, 0)$  and  $(r, 0, 0)$ . (d) 27 spheres of radius  $a = 0.795$  cm with relative permittivity  $\varepsilon = 2.6$ . The 27 spheres are in contact and stacked into a cube shape. The center of the sphere in the middle of the cube is  $(0, 0, 2a)$  cm. (e) A cylinder of radius  $a = 4$  cm, length  $2a$  with relative permittivity  $\varepsilon = 3.05$ . (f) A cube of size  $a = 2.5$  cm located at  $(-a/2, a/2, a/2)$  with relative permittivity  $\varepsilon = 2.45$  placed inside a cube of size  $2a$  cm located at  $(-2a/5, 2a/5, 5a/3)$  with relative permittivity  $\varepsilon = 1.45$ .

electromagnetic excitation  $\mathbf{E}_{l=1,\dots,L}^0$ . For each excitation  $l$ , the scattered field  $\mathbf{f}_l$  is measured on a surface  $\Gamma$  at  $M$  points and located outside the investigating domain  $\Omega$ . The aim of the inverse scattering problem is to find the relative permittivity of the object from the measured scattered field  $\mathbf{f}$ .

In this section, the authors present four different iterative methods to solve this nonlinear and ill-posed inverse scattering problem. The basic idea underlying iterative approaches to solve the inverse scattering problem is, starting from an initial guess, to adjust the parameter of interest gradually by minimizing some cost functional involving the data. For the sake of simplicity, symbolic notation is introduced to represent equations (3) and (5),

$$\mathbf{E}_l^d = \underline{\underline{B}}\chi\mathbf{E}_l, \tag{6}$$

$$\mathbf{E}_l = \mathbf{E}_l^0 + \underline{\underline{A}}\chi\mathbf{E}_l. \tag{7}$$

When varying the illumination  $\mathbf{E}_l^0$ , the matrices  $\underline{\underline{A}}$  and  $\underline{\underline{B}}$  do not change.

### 3.1. Conjugate gradient method

We first consider a linearized iterative inversion approach, the CGM, in which the internal field is considered as an auxiliary variable. In the CGM [14, 15], the forward problem is solved at each iteration step for the best available estimation of the parameter  $\chi$ . Fields  $\mathbf{E}_l$  within the investigating domain  $\Omega$  are thus considered as auxiliary variables and solely  $\chi$  is determined by minimizing an adequate cost function. A sequence  $\{\chi_n\}$  is built up according to the following updating relation

$$\chi_n = \chi_{n-1} + a_n d_n. \tag{8}$$

The updated  $\chi_n$  is deduced from the previous one  $\chi_{n-1}$  by adding a correction. This correction is composed of two terms: a scalar weight  $a_n$  and an updating direction  $d_n$ . Once the updating direction  $d_n$  is found, the scalar weight  $a_n$  is determined by minimizing the cost functional  $\mathcal{F}_n$  involving the residual error on the scattered field  $\mathbf{h}^{(1)}$  computed from the observation equation (equation (6))

$$\mathcal{F}_n(\chi_n) = \frac{\sum_{l=1}^L \|\mathbf{f}_l - \underline{\underline{B}}\chi_n \mathbf{E}_l\|_{\Gamma}^2}{\sum_{l=1}^L \|\mathbf{f}_l\|_{\Gamma}^2} = W_{\Gamma} \sum_{l=1}^L \|\mathbf{h}_{l,n}^{(1)}\|_{\Gamma}^2, \quad (9)$$

where  $\mathbf{h}^{(1)}$  and  $W_{\Gamma}$  are the residual error in the observation equation and a weighting coefficient, respectively:

$$\mathbf{h}_{l,n}^{(1)} = \mathbf{f}_l - \underline{\underline{B}}\chi \mathbf{E}_l \quad \text{and} \quad W_{\Gamma} = \left( \sum_{l=1}^L \|\mathbf{f}_l\|_{\Gamma}^2 \right)^{-1}. \quad (10)$$

The subscript  $\Gamma$  is included in the norm  $\|\cdot\|$  and later in the inner product  $\langle \cdot | \cdot \rangle$  in  $L^2$  to indicate the domain of integration. The field  $\mathbf{E}_l$  is the field that would be present in the investigating domain  $\Omega$  for the best available estimate of  $\chi$ , i.e.  $\mathbf{E}_l \approx \mathbf{E}_{l,n-1} = \left[ \underline{\underline{I}} - \underline{\underline{A}}\chi_{n-1} \right]^{-1} \mathbf{E}_l^0$ . Substituting the expression of the parameter of interest  $\chi_n$  derived from equation (8) into the cost functional described in equation (9) leads to a polynomial expression with respect to the scalar coefficient  $a_n$ . Doing so, the unique minimum of the cost function  $\mathcal{F}_n(a_n)$  is reached for

$$a_n = \frac{\sum_{l=1}^L \left\langle \mathbf{h}_{l,n-1}^{(1)} | \underline{\underline{B}}d_n \mathbf{E}_{l,n-1} \right\rangle_{\Gamma}}{\sum_{l=1}^L \|\underline{\underline{B}}d_n \mathbf{E}_{l,n-1}\|_{\Gamma}^2}, \quad (11)$$

where updating direction  $d_n$  is given by the standard Polack–Ribière conjugate gradient direction.

### 3.2. Contrast source inversion method: (CSI)

Contrary to the CGM, the CSI method is an iterative nonlinear technique in which the internal field is not fixed approximately at each iteration. The inversion problem is recast as a minimization of a cost functional

$$\mathcal{F}_n(\chi_n, \chi_n \mathbf{E}_{l,n}) = W_{\Gamma} \sum_{l=1}^L \|\mathbf{h}_{l,n}^{(1)}\|_{\Gamma}^2 + W_{\Omega} \sum_{l=1}^L \|\chi_n \mathbf{h}_{l,n}^{(2)}\|_{\Omega}^2, \quad (12)$$

where  $\mathbf{h}^{(2)}$  and  $W_{\Omega}$  are the residual error in the near-field equation and a weighting coefficient, respectively:

$$\mathbf{h}_{l,n}^{(2)} = \mathbf{E}_l^0 - \mathbf{E}_{l,n} + \underline{\underline{A}}\chi_n \mathbf{E}_{l,n} \quad \text{and} \quad W_{\Omega} = \left( \sum_{l=1}^L \|\chi_{n-1} \mathbf{E}_l^0\|_{\Omega}^2 \right)^{-1}. \quad (13)$$

The unknown parameters in these inversion methods are  $\chi$  and  $\chi \mathbf{E}_l$ , where  $\chi \mathbf{E}_l$  is the polarization distribution within the investigating domain  $\Omega$ . For more details on the CSI method, see [7].

### 3.3. The HM

The HM combines the advantages of the CGM and CSI. It has been introduced for scalar two-dimensional problems in [16–18]. In this paper, we extend it to the three-dimensional vectorial case.

The minimized cost function of the HM is the one used in the modified gradient method [6]

$$\mathcal{F}_n(\chi_n, \mathbf{E}_{l,n}) = W_\Gamma \sum_{l=1}^L \|\mathbf{h}_{l,n}^{(1)}\|_\Gamma^2 + \tilde{W}_\Omega \sum_{l=1}^L \|\mathbf{h}_{l,n}^{(2)}\|_\Omega^2, \quad (14)$$

where the weighting coefficient  $\tilde{W}_\Omega$  is given by

$$\tilde{W}_\Omega = \left( \sum_{l=1}^L \|\mathbf{E}_l^0\|_\Omega^2 \right)^{-1}. \quad (15)$$

Two sequences related to the contrast  $\chi$  and to the field inside the investigating domain  $\Omega$ ,  $\mathbf{E}_l$  are built up according to the following recursive relations

$$\chi_n = \chi_{n-1} + b_n d_n \quad (16)$$

$$\mathbf{E}_{l,n} = \mathbf{E}_{l,n-1} + a_{l,n}^v \mathbf{v}_{l,n} + a_{l,n}^w \mathbf{w}_{l,n}, \quad (17)$$

where  $\mathbf{v}_{l,n}$ ,  $\mathbf{w}_{l,n}$  and  $d_n$  are updating directions with respect to the total field  $\mathbf{E}_l$  and to the contrast  $\chi$ , respectively. The scalar coefficients  $a_{l,n}^v$ ,  $a_{l,n}^w$  and  $b_{l,n}$  are weights that are determined at each iteration step  $n$  such that they minimize the normalized cost functional given in equation (14). The minimization is accomplished using the Polak–Ribière conjugate gradient procedure [19]. The originality of the HM lies in the introduction of two search directions for the total field,  $\mathbf{w}_{l,n}$ , and  $\mathbf{v}_{l,n}$  which stem from the CGM and CSI methods, respectively. Basically,  $\mathbf{w}_{l,n}$  fastens the retrieval of the internal field (especially if the data are not too noisy and the target is not too contrasted) as in the CGM while  $\mathbf{v}_{l,n}$  brings the robustness to noise and the stability when handling strongly diffracting targets as in the CSI. They are written as,

$$\mathbf{v}_{l,n} = \mathbf{g}_{l,n;\mathbf{E}} + \gamma_{l,n;\mathbf{E}} \mathbf{v}_{l,n-1} \quad \text{with} \quad \gamma_{l,n;\mathbf{E}} = \frac{\langle \mathbf{g}_{l,n;\mathbf{E}}, \mathbf{g}_{l,n;\mathbf{E}} - \mathbf{g}_{l,n-1;\mathbf{E}} \rangle}{\|\mathbf{g}_{l,n-1;\mathbf{E}}\|^2} \quad (18)$$

$$\mathbf{w}_{l,n} = \tilde{\mathbf{E}}_l - \mathbf{E}_{l,n-1} \quad \text{with} \quad \tilde{\mathbf{E}}_l = (\underline{I} - \underline{A}\chi_{n-1})^{-1} \mathbf{E}_l^0, \quad (19)$$

where  $\mathbf{g}_{l,n;\mathbf{E}}$  is the gradient of the cost functional  $\mathcal{F}_n(\chi_n, \mathbf{E}_{l,n})$  with respect to  $\mathbf{E}_l$ , assuming  $\xi = \xi_{n-1}$  and  $\eta = \eta_{n-1}$  (see appendix A for details). Note that, similarly to the CGM, one forward problem has to be solved at each iteration.

To ameliorate the reconstruction, the authors have incorporated *a priori* information stating that both real and imaginary parts of the electrical susceptibility  $\chi$  are non-negative. Instead of retrieving a complex-valued function  $\chi_n$ , two real auxiliary functions  $\xi_n$  and  $\eta_n$  are reconstructed such that  $\chi_n = 1 + \xi_n^2 + i\eta_n^2 - \varepsilon_b$ , with  $\varepsilon_b$  the relative permittivity of the background. The real and the imaginary parts of the relative complex permittivity distribution are, herein, forced to be greater than unity and non-negative, respectively. The recursive relation with respect to the complex contrast function  $\chi_n$  is refined as

$$\xi_n = \xi_{n-1} + b_{n;\xi} d_{n;\xi} \quad \text{and} \quad \eta_n = \eta_{n-1} + b_{n;\eta} d_{n;\eta}. \quad (20)$$

The updating directions  $d_{n;\xi}$  and  $d_{n;\eta}$  are taken to be the standard Polak–Ribière conjugate gradient direction

$$d_{n;\xi} = g_{n;\xi} + \gamma_{n;\xi} d_{n-1;\xi} \quad \text{with} \quad \gamma_{n;\xi} = \frac{\langle g_{n;\xi}, g_{n;\xi} - g_{n-1;\xi} \rangle}{\|g_{n-1;\xi}\|^2}, \quad (21)$$

$$d_{n;\eta} = g_{n;\eta} + \gamma_{n;\eta} d_{n-1;\eta} \quad \text{with} \quad \gamma_{n;\eta} = \frac{\langle g_{n;\eta}, g_{n;\eta} - g_{n-1;\eta} \rangle}{\|g_{n-1;\eta}\|^2}, \quad (22)$$

where  $g_{n;\xi}$  and  $g_{n;\eta}$  are the gradients of the cost functional  $\mathcal{F}_n(\chi_n, \mathbf{E}_{l,n})$  with respect to  $\xi$  (respectively  $\eta$ ), evaluated at the  $n$ th step assuming that the total field inside the test domain does not change (see appendix A for details).

### 3.4. The positive conjugate gradient method: PCGM

Adding *a priori* information in the inversion procedure modifies significantly the reconstructed image [20]. Thus, for the purpose of comparison we have also developed a CGM under a positivity constraint. At each iteration, we now update  $\xi_n$  and  $\eta_n$  instead of  $\chi_n$ .

$$\xi_n = \xi_{n-1} + b_{n;\xi} d_{n;\xi} \quad \text{and} \quad \eta_n = \eta_{n-1} + b_{n;\eta} d_{n;\eta}, \quad (23)$$

where  $d_{n;\xi}$  and  $d_{n;\eta}$  are the descent directions obtained from the cost function equation (9) with  $\mathbf{E}_{l,n-1} = \left[ \mathbf{I} - \underline{\underline{A}} \chi_{n-1} \right]^{-1} \mathbf{E}_l^0$ . The scalar coefficients  $b_{n;\xi}$  and  $b_{n;\eta}$  are determined such that they minimize the normalized cost functional given in equation (9).

### 3.5. Parameter of interest

In all the presented methods, the sought parameter is the linear susceptibility  $\chi$  given by equation (2). Now, both the forward and inverse scattering problem can also be reformulated using the local electric field instead of the macroscopic electric field [8]. In this case, the parameter of interest sought would be the polarizability,  $\alpha(\mathbf{r}_j) = \frac{3d^3 \varepsilon(\mathbf{r}_j) - 1}{4\pi \varepsilon(\mathbf{r}_j) + 2}$  as proposed in [15]. We have implemented the two approaches and observed that they yielded similar results. The main argument in favor of the use of the macroscopic field and the linear susceptibility is that it is much easier to introduce the permittivity positivity *a priori* information with this formulation.

## 4. Numerical experiments

To investigate the performances of the different inversion methods sketched in the first section, we applied them to experimental data stemming from the microwave imaging set-up described in the special section [1, 21]. In this imaging, the targets are illuminated by an electromagnetic wave which can be assimilated to a plane wave. The scattered field is measured at 81 points on a sphere enclosing the targets with regular angular steps and with 36 incident directions taken in the  $(x, y)$  plane by rotating regularly over  $[2\pi]$  the emitting antenna about the  $z$ -axis. The background medium is homogeneous,  $\varepsilon_b = 1$ . With this illumination and detection configuration, a single scattering analysis estimates the resolution of the reconstruction to reach  $\lambda/4$  in the transverse  $(x, y)$  plane and  $\lambda/1.8$  in the  $(x, z)$  and  $(y, z)$  planes, where  $\lambda$  is the incident wavelength [20]. We considered five different targets, which are described in figure 1, and several incident frequencies from 3 to 8 GHz.

Prior to presenting the reconstructions obtained with the four different inversion methods described in the first section, it is important to discuss their convergence behavior and the stopping criterion. First, it is important to stress that the convergence of the three methods is not ensured mathematically. Yet, because of the minimization process, the cost functional of the CSI and HM are forced to decay at each iteration. Under some conditions, the CSI functional has even been shown to exhibit only one local minimum [22]. On the other hand, the decay of the cost functions of the CGM and PCGM is not automatic as the total field inside  $\Omega$  is estimated through a direct calculation, without minimizing the cost functional. We observed that, in all the considered examples, the cost functions of the CSI, CGM and PCGM had a similar behavior. After a certain number of iterations, they would decay slowly and continuously without visible changes on the reconstructions. The HM cost function, on the contrary, would rapidly reach a constant value which depended on the accuracy with which the scalar coefficients  $b_n$ ,  $a_{l,n}^v$  and  $a_{l,n}^w$  were optimized. We decided to stop the iterations of

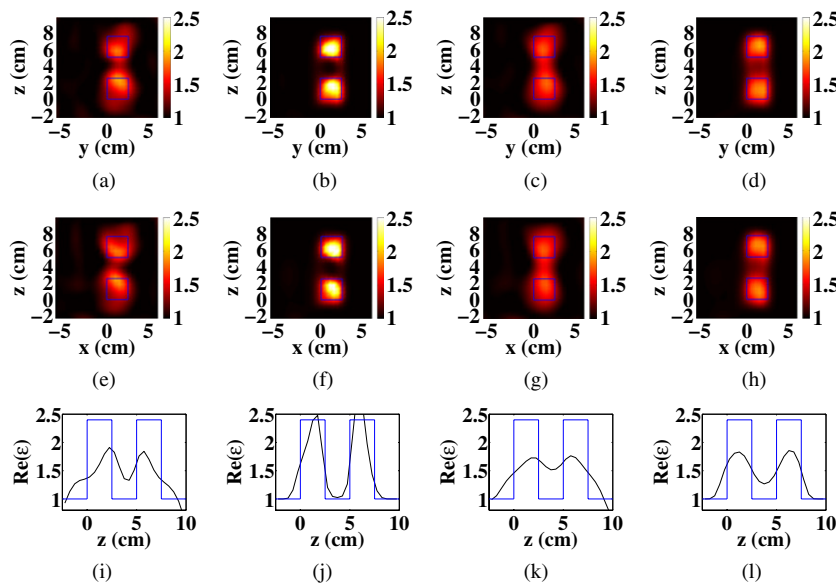


**Figure 2.** Reconstructed permittivity of the first target (two cubes along the  $z$ -axis) presented in figure 1 obtained with the different inversion methods from data obtained at 4 GHz. The first column corresponds to the CGM reconstruction; the second to the PCGM, the third to the CSI and the fourth to the HM. The first line represents the relative permittivity in the plane  $(y, z)$  at  $x = 0$ ; the second line the relative permittivity in the plane  $(x, z)$  at  $x = 0$  and the third line the relative permittivity versus  $z$  for  $x = y = 0$ .

the CGM, CSI and PCGM when the reconstruction did not evolve significantly anymore, while we stopped the HM iteration when the cost function reached the plateau. Note that, the cost functions of these methods being normalized differently, we cannot use their values as a stopping criterion.

## 5. Two cubes along the $z$ -direction: figure 1(b)

The first considered target is made up of two small cubes placed along the  $z$ -axis, figure 1(b). This simple object permits to test and validate the HM and to compare its performances to that of the CGM, PCGM and CSI in terms of convergence and computation time.

### 5.1. At low frequency : 4 GHz

We first inverted the data obtained at 4 GHz. At this frequency, the interdistance between the cube centers is about two third of the wavelength, which is above the single scattering resolution limit in the  $z$ -direction. As expected, both CGM and PCGM, and CSI and HM are able to resolve the two cubes, figure 2. Unsurprisingly, the results obtained with the PCGM and HM which uses the permittivity positivity *a priori* information are better than that given by the CGM and CSI which do not use this *a priori* information. With these data, which present a high signal-to-noise ratio, it appears that PCGM is better than the HM.

**Table 1.** Time of computation to get the final image and number of iterations needed for the four methods presented in this paper.

Frequency	Method	Number of iterations	Time by iteration (mn)	Total time (mn)
4 GHz	HM	28	6.35	178
4 GHz	PCGM	25	3.2	80
4 GHz	CGM	200	0.91	182
4 GHz	CSI	3000	0.72	2146
8 GHz	HM	13	8.46	110
8 GHz	PCGM	25	7.68	192
8 GHz	CGM	200	1.2	240
8 GHz	CSI	3000	0.83	2493

### 5.2. At high frequency: 8 GHz

We now study the data obtained at 8 GHz which exhibits a lower signal-to-noise ratio than those obtained at 4 GHz [21, 20]. As expected, all four methods retrieve accurately the two cubes. The PCGM and HM are once again slightly better than the CGM and CSI. However in this case, the PCGM is not as good as the HM as it reconstructs small ghost objects outside the targets and exhibits high permittivity peaks, whereas the HM reconstructed background is perfectly equal to one and its reconstructed permittivity is close to the actual value. We have observed in many examples that, with data presenting a high signal-to-noise ratio, the PCGM was the most efficient technique for retrieving the object's smallest details but that, on the other hand, it was the least robust to noise.

### 5.3. Computation time

The computation is carried on a single Intel processor with 3.2 GHz clock speed. For the two cubes' target, we give in table 1 the number of iterations, the computation time per iteration and the total computation time necessary to obtain the reconstructions plotted in figures (2) and (3). We observe that the CSI is much slower than all the other approaches. Indeed, although its iteration computation time is the smallest, as one does not need to solve any forward problem, the number of iterations required to obtain a converged result is huge. On the other hand, the CGM, PCGM and HM have a relatively long computation time for each iteration, but this issue is largely compensated by the small number of iterations required for getting a converged result. Actually, solving the forward problem, which used to be very time consuming, is now performed surprisingly fast thanks to recent algorithmic progress [23, 12]. The CGM iteration is faster than the PCGM and HM because it does not require one to optimize iteratively the scalar coefficients of the recursive relations.

Note that for the CGM, PCGM and HM the iteration computation time increases with illumination frequency. Indeed, the time required to solve the direct problem depends directly on the object size with respect to the illumination wavelength. At 8 GHz, convergence of the PCGM takes more iterations than at 4 GHz because of the lower signal-to-noise ratio. At this frequency, the HM is the fastest method. The behavior of the residual error versus the iteration is plotted for each method and for both frequencies in figure 4. We observe that, except for the PCGM which is most sensitive to noise, the high frequency data yield a better residue than the low frequency data. These curves are emblematic of the cost function behavior of these methods. The HM residue quickly reaches a constant value plateau while the three other methods decrease monotonically and slowly after a few iterations. We recall that one cannot compare the values of the residues as each method has its own normalization.

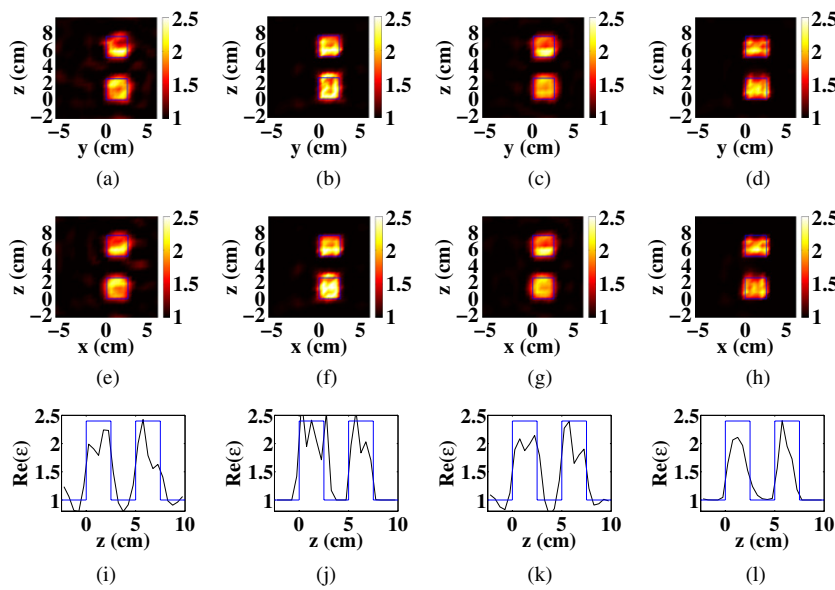


Figure 3. Same as in figure 2 but at 8 GHz.

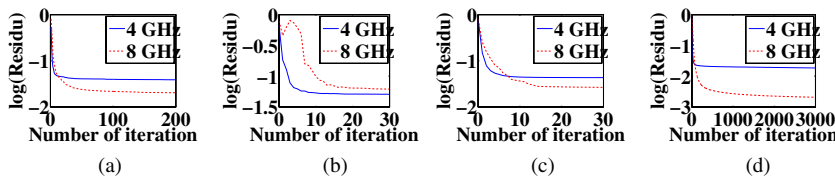


Figure 4. Behavior of the cost functional for the four different methods at 4 GHz and 8 GHz. (a) CGM. (b) PCGM. (c) HM. (d) CSI.

We now turn to four other targets which are more difficult to invert as they are larger than the wavelength of illumination or have a complex structure. Three of them, figure 1(c)–(e) were in the database of the special section [1] and most methods failed to reconstruct them. They permit us to investigate the performances of the techniques in terms of reconstruction accuracy and robustness to noise.

## 6. Two spheres in contact: figure 1(c)

### 6.1. Two spheres in contact at 5 GHz

In this section we study two spheres in contact. This configuration is particularly difficult as the contact is punctual and the two spheres form an object larger than the wavelength of illumination for the frequency of 5 GHz. The CGM and PCGM fail to converge and the reconstructions presented in figure 5 correspond to those obtained for the best residue, i.e. the 43rd iteration and 2nd iteration, respectively. This example highlights the main problem of the CGM and PCGM, in which the cost function is not forced to decrease.

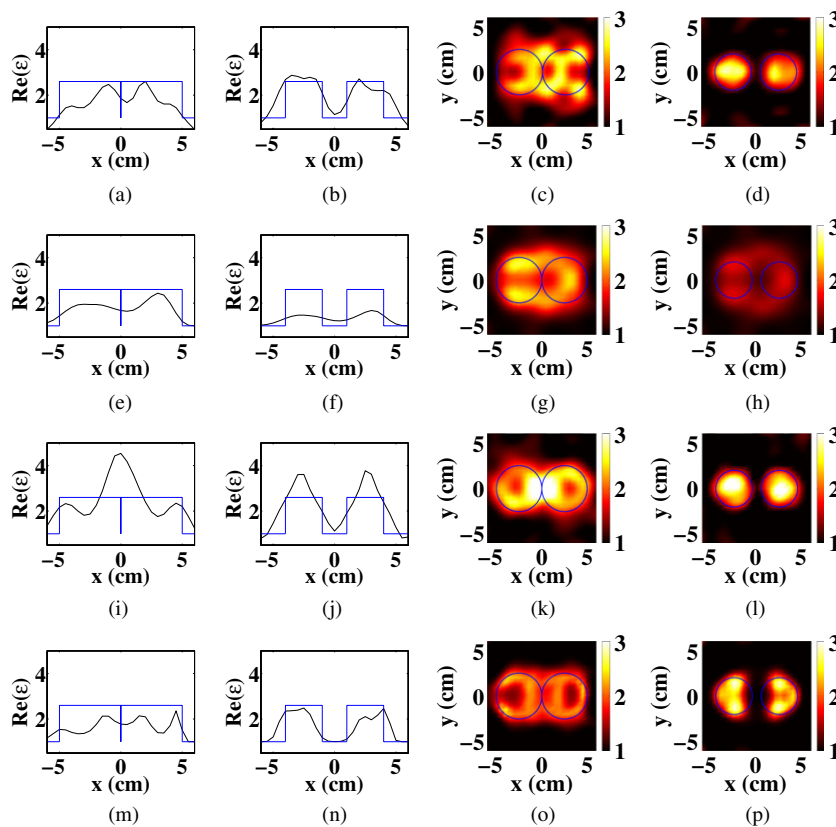


**Figure 5.** Reconstructed permittivity map of the second target (two spheres in contact) depicted in figure 1 obtained with the four inversion methods from data obtained at 5 GHz. First line corresponds to the CGM; second line to the PCGM; third line to the CSI; fourth line to the HM. First and second column : cut of the relative permittivity versus  $x$  for  $y = z = 0$  and for  $y = 0$  and  $z = a/2$ , respectively. Third and fourth column: map of relative permittivity in the  $(x, y)$  plane for  $z = 0$  and  $z = a/2$ , respectively.

On the other hand, the CSI method, third line of figure 5, converges and it retrieves the shape of the two spheres. Yet, the reconstructed relative permittivity is too high, especially close to the contact point. Similarly, the HM gives a map of permittivity which roughly fits the actual shape of the spheres while the permittivity at the contact point is not overestimated.

We have observed that if the frequency is increased up to 6 GHz, the HM fails to find the object and only the CSI gives a meaningful result; and for frequencies above 7 GHz all the methods fail.

### 6.2. Two spheres in contact: frequency hopping

To ameliorate the reconstruction, one can use the data obtained at different frequencies and perform a frequency hopping procedure. At each frequency, the object's initial estimate introduced in the inversion algorithm is given by the reconstruction obtained at the preceding (lower) frequency. Figure 6 presents the results obtained using the frequency hopping HM for the sequence 3–8 GHz. We considered only the HM because the CGM and PCGM failed

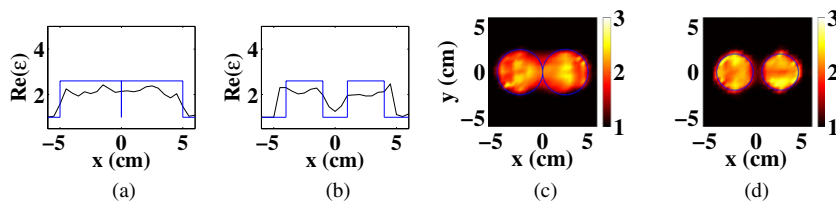


**Figure 6.** Same as figure 5 but the reconstruction is obtained with the HM via a frequency hopping procedure applied to the data measured at 3–8 GHz. (a) Relative permittivity versus  $x$  for  $y = z = 0$  and (b) for  $y = 0$  and  $z = a/2$ . Map of relative permittivity in the  $(x, y)$  plane for (c)  $z = 0$  and (d)  $z = a/2$ .

to converge at 5 GHz and because the CSI method was much too long. It took 22 h for the HM to reconstruct the spheres while we estimated the CSI time to be 9 days. We observe in figure 6 that the HM combined with frequency hopping gives an accurate reconstruction of the two spheres. With good initial estimates, the convergence issue for frequencies above 6 GHz has disappeared. This example stresses the interest (in particular with respect to computation time) and the robustness of the HM. Note that at 8 GHz the object size is about three wavelengths.

## 7. Aggregate of 27 spheres: figure 1(d)

We now consider a complex structure made up of 27 spheres that are stacked into a cube and illuminated at i.e. 8 GHz. At this frequency, the diameter of the spheres is roughly half the wavelength. We observe that all the methods yield similar results, as shown in figure 7. In agreement with the single scattering resolution analysis, the spheres are accurately resolved in the  $(x, y)$  plane, while they are poorly visible in the  $(x, z)$  or  $(y, z)$  planes. Note that the important noise at this frequency clearly causes the performance of the PCGM to deteriorate.

## 8. Cylinder: figure 1(e)

### 8.1. Cylinder at 3 GHz

Here we consider a cylinder larger than the illumination wavelength (at 3 GHz), figure 1(e), and with high relative permittivity,  $\varepsilon = 3.05$ . Because of its size and high relative permittivity, most inversion methods presented in the special section in [1] failed to reconstruct this target. Satisfactory results were obtained only with a regularized CSI by using simultaneously all the illumination frequencies [24] and with a regularized distorted Born approach [25] using frequency hopping. Using solely the data at 3 GHz, we observe in figure 8 that the result obtained with the HM is better than that obtained with the non-regularized CSI and the PCGM, and is similar to the result obtained in [25] with regularized distorted Born. Note that the CGM did not converge at 3 GHz and that all the methods failed to converge at 4 GHz.

### 8.2. Cylinder at 4 GHz: frequency hopping

Taking advantage of the HM's short computation time, we applied the HM frequency hopping algorithm to the [3, 3.5, 4 GHz] frequency sequence. In this case, the HM converged even at

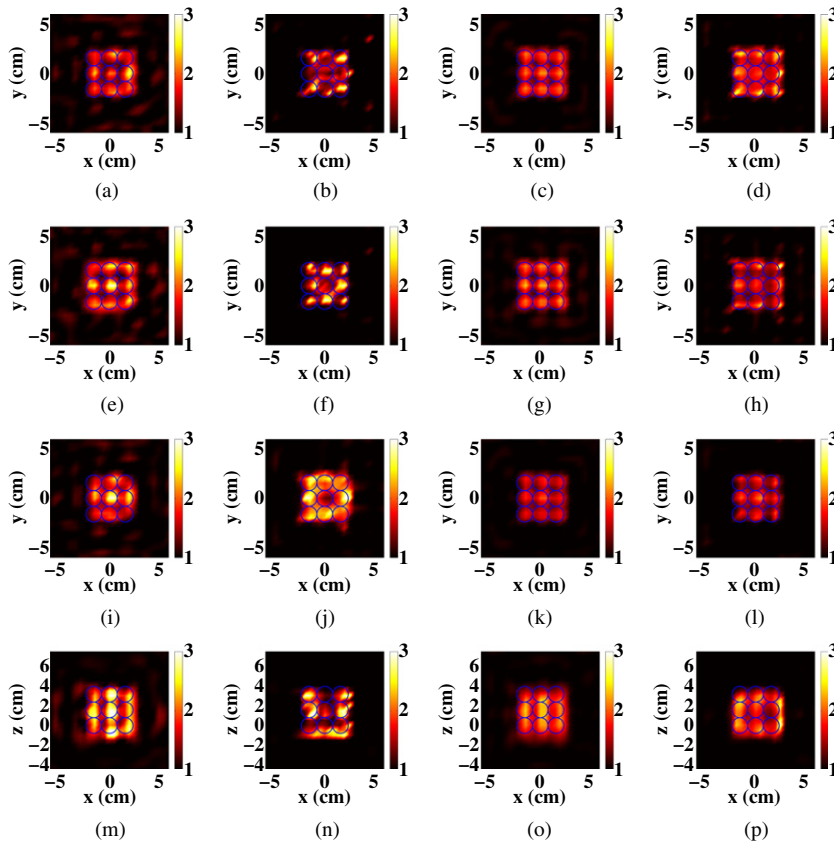


**Figure 7.** Reconstructed relative permittivity of the third target (27 spheres in a cube) depicted in figure 1 obtained by the four inversion methods at 8 GHz. First column corresponds to the CGM; second column to the PCGM; third column to the CSI; fourth column to the HM. Map of relative permittivity in the  $(x, y)$  plane for  $z = 0$  (first line),  $z = 2a$  (second line) and  $z = 4a$  (third line). Fourth line: map of relative permittivity in the  $(x, z)$  plane for  $y = 0$ .

4 GHz and we obtained a better reconstruction than at 3 GHz, figure 9. This result is similar to that obtained in [25] with regularized distorted Born under frequency hopping.

### 9. Inhomogeneous target at 8 GHz: figure 1(f)

In this last example, we consider an inhomogeneous object made up of two nested cubes, a cube of  $\varepsilon = 2.4$  set inside a cube of  $\varepsilon = 1.45$ . The small internal cube is slightly off center. At, i.e., 8 GHz the largest distance between the edges of the internal and external cubes is about  $\lambda/2.5$  in the  $(x, y)$  plane, while the smallest distance is about  $\lambda/3.75$ . We observe in figure 10 that the HM and PGCM are able to distinguish the change of permittivity along the largest distance between the cube edges but fail to retrieve it along the smallest distance. On the other hand, the CGM and CSI failed to retrieve the permittivity change on both sides. This example highlights the advantage of injecting *a priori* information into the reconstruction procedures to ameliorate the resolution. Note that, as usual, the PCGM exhibits spurious high permittivity peaks that can be attributed to the high level of noise at this frequency.

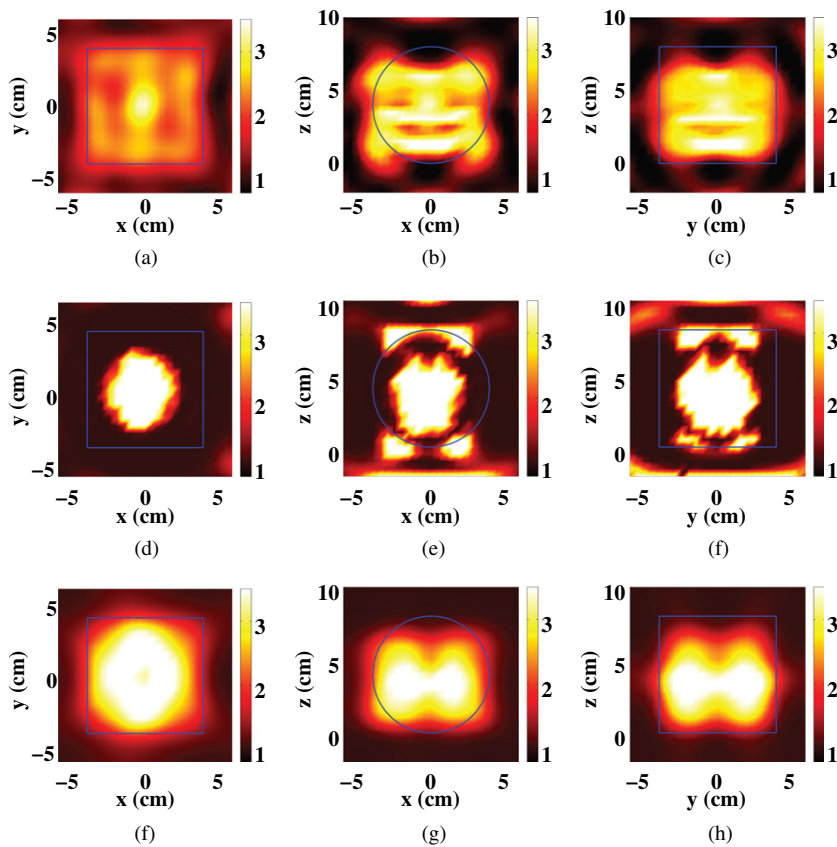


**Figure 8.** Reconstructed permittivity of the fourth target (large cylinder) depicted in figure 1 obtained by the CSI (a,b,c), the PCGM (d,e,f) and HM (g,h,i) from data obtained at 3 GHz. The CGM does not give any result for this target. Map of relative permittivity in the  $(x, y)$  plane at  $z = 0$  (a), (d) and (g); in the  $(x, z)$  plane at  $y = 0$  (b), (e) and (h); in the  $(y, z)$  plane at  $x = 0$  (c), (f) and (i).

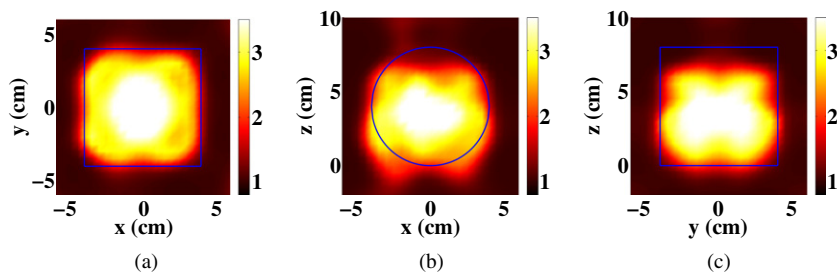


**Figure 9.** Same as figure 8 but with the HM using frequency hopping from 3, 3.5 and 4 GHz. Map of relative permittivity in the  $(x, y)$  plane at  $z = 0$  (a); in the  $(x, z)$  plane at  $y = 0$  (b); in the  $(y, z)$  plane at  $x = 0$  (c).

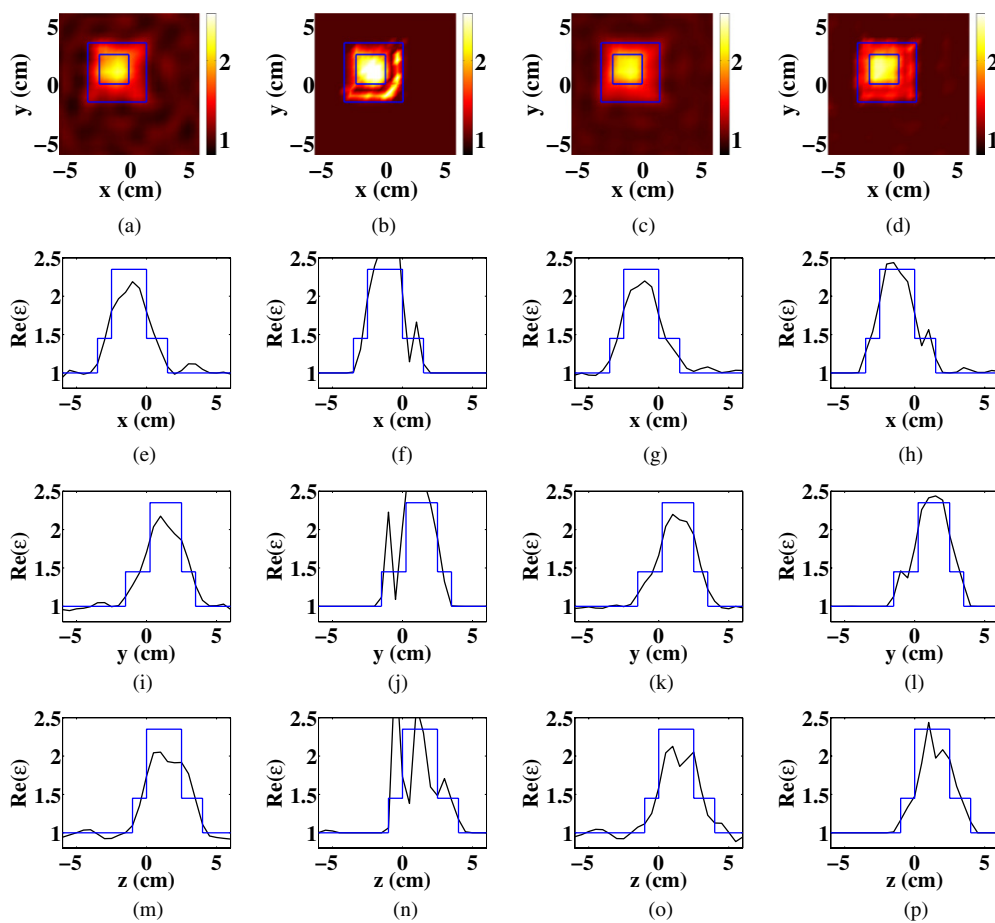


**Figure 10.** Reconstructed relative permittivity of the fifth target (inhomogeneous cube) depicted in figure 1 obtained with the four inversion methods at 8 GHz. First column corresponds to the CGM, second column to the PCGM, third column to the CSI and fourth column to the HM. (a)–(d) map of relative permittivity in the  $(x, y)$  plane at  $z = 10$  mm; (e)–(h) relative permittivity versus  $x$  for  $y = 10$  mm and  $z = 15$  mm; (i)–(l) relative permittivity versus  $y$  for  $x = -15$  mm and  $z = 10$  mm; (m)–(p) relative permittivity versus  $z$  for  $x = -15$  mm and  $y = 15$  mm.

## 10. Conclusion

In electromagnetic wave imaging, the field scattered by the target is usually nonlinearly linked to the unknown permittivity map. We have adapted to the three-dimensional vectorial case a hybrid inversion method that combines the advantages of nonlinearized and linearized inversion techniques and investigated its performance with experimental microwave data. We have shown that the hybrid method (HM) was dramatically faster than the nonlinearized technique and significantly more efficient than the linearized techniques for reconstructing large objects or for dealing with noisy data. Hence, we believe that the HM is an interesting approach for electromagnetic digital imaging. It is particularly appropriate for performing frequency hopping procedures (because of its short computation time) and for imaging in the optical domain (where the data are often corrupted with an important noise).

## Acknowledgement

The authors are grateful to the HIPE team of the Fresnel Institute for providing the experimental data. More details about the experimental configuration can be found in [26, 27].

## Appendix. Formulae for the gradients used in the HM and PCGM

The gradients used in the HM are the gradients of the functional

$$\begin{aligned} \mathcal{F}_n(\xi_n, \eta_n, \mathbf{E}_{l,n}) = & W_\Gamma \sum_{l=1}^L \|\mathbf{f}_l - \underline{\underline{B}}(1 + \xi_n^2 + i\eta_n^2 - \varepsilon_b)\mathbf{E}_{l,n}\|_\Gamma^2 \\ & + \tilde{W}_\Omega \sum_{l=1}^L \|\mathbf{E}_l^0 - \mathbf{E}_{l,n} + \underline{\underline{A}}(1 + \xi_n^2 + i\eta_n^2 - \varepsilon_b)\mathbf{E}_{l,n}\|_\Omega^2. \end{aligned} \quad (\text{A.1})$$

This cost function involves two residuals errors:

$$\mathbf{h}_{l,n}^{(1)} = \mathbf{f}_l - \underline{\underline{B}}\chi_n\mathbf{E}_{l,n} \quad \text{and} \quad \mathbf{h}_{l,n}^{(2)} = \mathbf{E}_l^0 - \mathbf{E}_{l,n} + \underline{\underline{A}}\chi_n\mathbf{E}_{l,n}, \quad (\text{A.2})$$

with  $\chi_n = 1 + \xi_n^2 + i\eta_n^2 - \varepsilon_b$ .

The gradients according to  $\xi_n$  and  $\eta_n$  are given by

$$g_{n;\xi} = 2\xi_{n-1} \text{Re} \left[ \tilde{W}_\Omega \sum_{l=1}^L \overline{\mathbf{E}}_{l,n-1} \cdot \underline{\underline{A}}^\dagger \mathbf{h}_{l,n-1}^{(2)} - W_\Gamma \sum_{l=1}^L \overline{\mathbf{E}}_{l,n-1} \cdot \underline{\underline{B}}^\dagger \mathbf{h}_{l,n-1}^{(1)} \right], \quad (\text{A.3})$$

$$g_{n;\eta} = 2\eta_{n-1} \text{Im} \left[ \tilde{W}_\Omega \sum_{l=1}^L \overline{\mathbf{E}}_{l,n-1} \cdot \underline{\underline{A}}^\dagger \mathbf{h}_{l,n-1}^{(2)} - W_\Gamma \sum_{l=1}^L \overline{\mathbf{E}}_{l,n-1} \cdot \underline{\underline{B}}^\dagger \mathbf{h}_{l,n-1}^{(1)} \right]. \quad (\text{A.4})$$

The gradient according to  $\mathbf{E}_{l,n}$  is given by

$$g_{l,n;\mathbf{E}} = \tilde{W}_\Omega \left[ \overline{\chi_{n-1}} \underline{\underline{A}}^\dagger \mathbf{h}_{l,n-1}^{(2)} - \mathbf{h}_{l,n-1}^{(2)} \right] - W_\Gamma \overline{\chi_{n-1}} \underline{\underline{B}}^\dagger \mathbf{h}_{l,n-1}^{(1)}. \quad (\text{A.5})$$

In these three equations, the overbar denotes the complex conjugate and  $\underline{\underline{M}}^\dagger$  is the adjoint operator of the operator  $\underline{\underline{M}}$ .

## References

- [1] Litman A and Crocco L 2009 Testing inversion algorithms against experimental data: 3D targets *Inverse Problems* **25** 020201
- [2] Joachimowicz N, Pichot C and Hugonin J-P 1991 Inverse scattering: an iterative numerical method for electromagnetic imaging *IEEE Trans. Antennas Propag.* **39** 1742–53
- [3] Belkebir K, Elissalt J M, Geffrin J M and Pichot C 1996 Newton–Kantorovich and modified gradient inversion algorithms applied to Ipswich data *IEEE Antennas Propag. Mag.* **38** 41–4
- [4] Chew W C and Wang Y M 1990 Reconstruction of two-dimensional permittivity distribution using distorted Born iterative method *IEEE Trans. Med. Imaging* **9** 218–25
- [5] Remis R F and van den Berg P M 2000 On the equivalence of the Newton–Kantorovich and distorted Born methods *Inverse Problems* **16** L1–4
- [6] Kleinman R E and van den Berg P M 1992 A modified gradient method for two-dimensional problems in tomography *J. Comput. Appl. Math.* **42** 17–35
- [7] Abubakar A and van den Berg P M 2002 The contrast source inversion method for location and shape reconstructions *Inverse Problems* **18** 495–510
- [8] Chaumet P C, Sentenac A and Rahmani A 2004 Coupled dipole method for scatterers with large permittivity *Phys. Rev. E* **70** 036606
- [9] Chaumet P C, Rahmani A and Nieto-Vesperinas M 2005 Photonic force spectroscopy on metallic and absorbing nanoparticles *Phys. Rev. B* **71** 045425

- [10] Chaumet P C and Rahmani A 2009 Electromagnetic force and torque on magnetic and negative-index scatterers *Opt. Express* **17** 2224–34
- [11] Jackson J D 1975 *Classical Electrodynamics* 2nd edn (New York: Wiley)
- [12] Chaumet P C and Rahmani A 2009 Efficient iterative solution of the discrete dipole approximation for magneto-dielectric scatterers *Opt. Lett.* **34** 917–9
- [13] Tang J, Shen Y, Zheng Y and Qiu D 2004 An efficient and flexible computational model for solving the mild slope equation *Coast. Eng.* **51** 143–54
- [14] Chaumet P C and Belkebir K 2009 Three-dimensional reconstruction from real data using a conjugate gradient-coupled dipole method *Inverse Problems* **25** 024003
- [15] Belkebir K, Chaumet P C and Sentenac A 2005 Super-resolution in total internal reflection tomography *J. Opt. Soc. Am. A* **22** 1889–97
- [16] Belkebir K and Tijhuis A G 2001 Modified<sup>2</sup> gradient method and modified Born method for solving a two-dimensional inverse scattering problem *Inverse Problems* **17** 1671–88
- [17] Dubois A, Belkebir K and Saillard M 2005 Retrieval of inhomogeneous targets from experimental frequency diversity data *Inverse Problems* **21** S65–79
- [18] Belkebir K, Bonnard S, Pezin F, Sabouroux P and Saillard M 2000 Validation of 2D inverse scattering algorithms from multi-frequency experimental data *J. Electromagn. Waves Appl.* **14** 1637–67
- [19] Press W H, Flannery B P, Teukolski S A and Vetterling W T 1986 *Numerical Recipes. The Art of Scientific Computing* (Cambridge: Cambridge University Press)
- [20] Chaumet P C, Belkebir K and Sentenac A 2009 Experimental microwave imaging of three-dimensional targets with different inversion procedures *J. Appl. Phys.* **106** 034901
- [21] Geffrin J M and Sabouroux P 2009 Continuing with the Fresnel database: experimental setup and improvements in 3D scattering measurements *Inverse Problems* **25** 024001
- [22] van den Berg P M and Abubakar A 2001 Contrast source inversion method: state of art *Prog. Electromagn. Res.* **34** 189–218
- [23] Goodman J J and Flatau P J 2002 Application of fast-Fourier-transform techniques to the discrete-dipole approximation *Opt. Lett.* **16** 1198–200
- [24] Li A, Abubakar M and van den Berg P M 2009 Application of the multiplicative regularized contrast source inversion method on 3D experimental Fresnel data *Inverse Problems* **25** 024006
- [25] Yu M Y C and Liu Q H 2009 Reconstruction of 3D objects from multi-frequency experimental data with a fast DBIM-bCGS method *Inverse Problems* **25** 024007
- [26] Geffrin J-M, Chaumet P C, Eyraud C, Belkebir K and Sabouroux P 2008 Electromagnetic three-dimensional reconstruction of targets from free space experimental data *Appl. Phys. Lett.* **92** 194103
- [27] Eyraud C, Geffrin J-M, Sabouroux P, Chaumet P C, Torteil H, Giovannini H and Litman A 2008 Validation of 3D bistatic microwave scattering measurement setup *Radio Sci.* **43** RS4018